scientific reports

Check for updates

OPEN

Tuning band gap and enhancing optical functions of $AGeF_3$ (A = K, Rb) under pressure for improved optoelectronic applications

Md. Safin Alam[1], Md Saiduzzaman[1]✉, Arpon Biswas[1], Tanjun Ahmed[1], Aldina Sultana[1] & Khandaker Monower Hossain[2]✉

The current study diligently analyzes the physical characteristics of halide perovskites $AGeF_3$ (A = K, Rb) under hydrostatic pressure using density functional theory. The goal of this research is to reduce the electronic band gap of $AGeF_3$ (A = K, Rb) under pressure in order to improve the optical characteristics and assess the compounds' suitability for optoelectronic applications. The structural parameters exhibit a high degree of precision, which correlates well with previously published work. In addition, the bond length and lattice parameters decrease significantly leading to a stronger interaction between atoms. The bonding between K(Rb)–F and Ge–F reveal ionic and covalent nature, respectively, and the bonds become stronger under pressure. The application of hydrostatic pressure demonstrates remarkable changes in the optical absorption and conductivity. The band gap becomes lower with the increment of pressure, resulting in better conductivity. The optical functions also predict that the studied materials might be used in a variety of optoelectronic devices operating in the visible and ultraviolet spectrum. Interestingly, the compounds become more suitable to be used in optoelectronic applications under pressure. Moreover, the external pressure has profound dominance on the mechanical behavior of the titled perovskites, which make them more ductile and anisotropic.

Cubic perovskites have obtained substantial preference from researchers and scientists over the last few years. The versatile applicability of these perovskites in multiple sectors, e.g., semiconductors, sensors, superconductivity, photovoltaic cells, optoelectronic devices, and LEDs (light-emitting devices)[1–3] puts them in the center of attention. As a result, the researchers conducted both experimental and theoretical studies[4–7] on the physical behavior of perovskite materials to create new possibilities for their applications in various optoelectronic fields. Interestingly, the improvement of perovskite solar cells (PSCs) has been accelerated, resulting in power conversion efficiency (PCE) of 22.1%[8]. Till now, the best PCE of 25.2% is recorded for Pb-based perovskite solar cells[9] but have less life span caused by humidity, moisture, temperature, and UV light[10]. On the other hand, the lead-free tin halide perovskite incorporated with ethylammonium iodide exhibited the PCE of ~ 13%[11]. At initial stages, metallic Pb^{2+}-based organic PSCs i.e., $CH_3NH_3PbI_3$ (or $MAPbX_3$) were developed[12–14]. But the toxicity of these organic compounds created major disadvantages. Pb is a recognized toxin, creating a number of obstacles[15]. In addition, organic MA^+ cations cause serious environmental drawbacks, making the manufacturing process extremely risky and harmful[16]. In order to nullify the toxicity, non-toxic cations, like Ge^{2+} and Sn^{2+} have replaced Pb^{2+} cation, and/or K^+, Rb^+, and Cs^+ cations have used to replace the organic counterpart[15,17–19]. Therefore, a new formation of ABX_3 has appeared in which A, B, and C denote the monovalent cation, divalent cation, and halogen anion, respectively. Inorganic perovskites based on Ge have emerged as a possible alternative of Pb, because they possess superior optical absorption and conductivity as compared to Pb-based perovskites[20]. At ambient temperature, Ge-based perovskites do not exhibit any phase transformation[21,22]. Besides, K and Rb have shown promising potential for photo-voltaic applications[23]. Jain et al.[24] have utilized the first-principle calculations on $RbSn(Cl,Br)_3$ perovskites to evaluate prominent band gap suitable for photovoltaics. The monovalent cation K^+-based perovskites have potential to be utilized in solar cells because of high absorption and configurable band gap[20,22,25]. In recent studies, the inorganic halide perovskites have been recognized as a reliable material for solar cell applications[25,26]. For the purpose of enhancing physical properties of halide perovskites,

[1]Department of Materials Science and Engineering, Khulna University of Engineering & Technology (KUET), Khulna 9203, Bangladesh. [2]Department of Materials Science and Engineering, University of Rajshahi, Rajshahi 6205, Bangladesh. ✉email: msaiduzzaman@mse.kuet.ac.bd; monower37@gmail.com

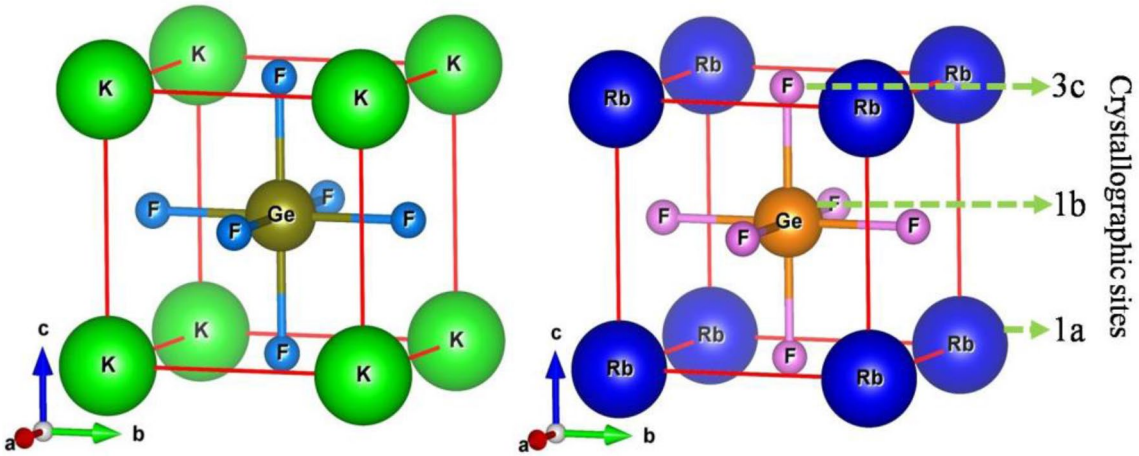

Figure 1. The optimized crystal structure of halide perovskites $KGeF_3$ and $RbGeF_3$.

Compound	Calculated data	Pressure (GPa)			
		0	10	20	30
$KGeF_3$	a (Å)	4.451 [This work]	4.243	4.117	4.023
		4.46[31]			
	V (Å^3)	88.18	76.37	69.78	65.11
	ΔE_f (eV/atom)	−4.63	−4.57	−4.44	−4.30
$RbGeF_3$	a (Å)	4.490 [This work]	4.281	4.154	4.061
		4.49[31]			
	V (Å^3)	90.52	78.46	71.68	66.97
	ΔE_f (eV/atom)	−4.62	−4.55	−4.43	−4.28

Table 1. Calculated lattice constant (a), unit cell volume (V), and formation energy (ΔE_f) of $AGeF_3$ (A = K, Rb) at various applied pressures.

the application of hydrostatic pressure has demonstrated tremendous results[27–32]. Usually, hydrostatic pressure modifies the lattice parameters[33], displacement of cation and anion[34,35], rotation of octahedral cages[36], phase transitions[37,38], etc. In the case of metal halides, structural properties, like lattice constants and unit cell volume decrease with increasing pressure[29,32]. Identical behavior can be detected in halide perovskites as well. In recent works, inorganic halide perovskites, such as $KCaCl_3$[39], $CsGeI_3$[30], $RbYbF_3$[40], and $CsGeI_3$[41] have shown reduction in band gap under hydrostatic pressure, resulting an improvement of conductivity. In addition, the application of pressure can remarkably develop the optical parameters of halide perovskites, enhancing the functionality in optoelectronic fields. Therefore, the motive of present work is to evaluate and examine the changes of various physical features of halide perovskites $AGeF_3$ (A = K, Rb) after applying hydrostatic pressure. More specifically, this study has analyzed the structural, electronic, optical, and mechanical properties of $AGeF_3$ (A = K, Rb) using first-principle calculations to observe whether the application of hydrostatic pressure has made them more appealing to optoelectronic fields or not.

Results and discussion

Structural properties. The geometry optimization states that the selected compounds $AGeF_3$ (A = K, Rb) under study crystallized in cubic cell that have the space group *Pm*-3*m* (#221). In the unit cell, the A (= K, Rb), Ge, and F atoms are located at the corner, body center, and face center, respectively, with the Wyckoff positions 1a (0, 0, 0), 1b (0.5, 0.5, 0.5), and 3c (0, 0.5, 0.5), respectively. The optimized crystal structure of $AGeF_3$ (A = K, Rb) with crystallographic sites is illustrated in Fig. 1. The evaluated lattice constant of $KGeF_3$ at ambient pressure is 4.451 Å (Table 1), which is relatively closer to the reference study (4.46 Å)[20]. The deviation value of 0.2% presents the high accuracy of this study. For $RbGeF_3$, the lattice constant is 4.490 Å (Table 1), showing no deviation from the previous work (4.49 Å)[20]. The hydrostatic pressure ranging from 0 to 30 GPa is applied on both compounds to calculate the structural parameters as given in Table 1. The application of pressure demonstrates a significant effect on the structural parameters. The changes of relative lattice constants and unit cell volume with respect to the hydrostatic pressure are illustrated in Fig. S1a,b, respectively. The plotted graphs reveal the reduction of both lattice constant and unit cell volume under linear ascending of applied pressure. This decreasing tendency of lattice parameters under hydrostatic pressure indicates the reduction of bond length (Table 2) within the compounds. In order to justify the phase stability of $AGeF_3$ (A = K, Rb) under pressure, the formation energy (ΔE_f) is calculated using the following equation and recorded in Table 1.

Pressure (GPa)	Bond length (Å)			
	$KGeF_3$		$RbGeF_3$	
	Ge–F	K–F	Ge–F	Rb–F
0	3.14714	2.22537	3.17491	2.24500
10	3.00043	2.12162	3.02725	2.14059
20	2.91083	2.05827	2.93745	2.07709
30	2.84527	2.01191	2.87188	2.03072

Table 2. Estimated bond lengths in $AGeF_3$ (A = K, Rb) at various applied pressures.

$$\Delta E_f(AGeF_3) = \frac{[E_{tot.}(AGeF_3) - E_s(A) - E_s(Ge) - 3E_s(F)]}{N}. \quad (1)$$

Here, E_s(A), E_s(Ge), and E_s(F) are the energy of A (= K, Rb), Ge, and F atoms, respectively, whereas, $E_{tot}(AGeF_3)$ represents the unit cell total energy of $AGeF_3$, and N is the number of atoms in the unit cell. The negative values of ΔE_f at all applied pressures reveal the thermodynamic stability of titled halide systems[42].

Electronic properties. The assessment a material's electronic nature requires the understanding of its band structure and density of states. The band structures of $KGeF_3$ and $RbGeF_3$ at different applied pressures are shown in Figs. 2 and 3, respectively. The horizontal dotted line at 0 eV denotes the Fermi level (E_F). At 0 GPa, the valence band maximum (VBM) and conduction band minimum (CBM) indicated by green and red lines, respectively, of both compounds are noticed at R point of the Brillouin zone. Therefore, a direct band gap (E_g) of 1.98 eV is found for $KGeF_3$, while it is 2.012 eV for $RbGeF_3$. The E_g values found for $AGeF_3$ (A = K, Rb) are quite consistent with the theoretical values obtained using the GGA-PBE approximation[19]. With increasing pressure, the CBM of both compounds begin to move towards the E_F, resulting in a reduction of E_g. At 30 GPa, the E_g of $KGeF_3$ falls to 0.16 eV, while it is 0.26 eV for $RbGeF_3$. The reduction of E_g under pressure for both compounds is graphically presented in Fig. S2. There exists an inverse relationship between band gap and external pressure[43], which can increase the potential between electron and ion responsible for reducing lattice parameters (Table 1). The band gap at the Brillouin zone symmetry point shrinks when the lattice parameter is reduced. The reduction of E_g allows easy transport of electrons from valence band to conduction band. As a result, the optical absorption and conductivity may become higher beneficial for optoelectronic applications.

Furthermore, the total density of states (TDOS) of $AGeF_3$ (A = K, Rb) are computed and illustrated in Fig. S3a,b to explicate the band structures. The vertical dashed line at 0 eV denotes the E_F. There observe no TDOS value at E_F for both compounds under all applied pressures, which also reflects the semiconducting nature of them. There is a significant pressure influence on TDOS in the conduction band, where all the sharp peaks gradually move towards the E_F as pressure increases. This peak shifting is responsible for the band gap shrinking under pressure, which is also appeared in the band structures at R point. However, the partial density of states (PDOS) is crucial to obtain the atomic contribution of a material for making its band structure. It is evident from Figs. 4 and 5 that the valence band of both compounds near the E_F mostly originate from Ge-4s and F-2p orbitals with small amount of Ge-4p orbital. On the other hand, the conduction band results from K-4s (Rb-5s), K-4p (Rb-4p), Ge-4s, Ge-4p, and F-2p states. It is apparent that the Ge-4p orbital is mainly responsible for narrowing the E_g in both compounds. The hybridization between Ge-4p and F-2p is promoted by raising external pressure, which raises the conduction bands towards the E_F and reduces the band gap. Furthermore, the shortening of Ge–F bond length in response to pressure (Table 2) could improve the hybridization between Ge-4p and F-2p orbitals in the conduction band, which lowers the CBM at R point of the Brillouin zone (Figs. 2, 3). Hence, the band gap of $KGeF_3$ ($RbGeF_3$) reduces from 1.98 (2.012 eV) to 0.16 eV (0.26 eV).

Charge density mapping helps to visualize the charge distribution around atoms and bonding nature of the compounds. Figures 6 and 7 illustrate the charge density mapping of $AGeF_3$ (A = K, Rb) along the crystallographic planes (100) and (200). The right side scales indicate the electron density, in which low and high intensity are imparted by blue and red colors, respectively. At ambient pressure, K(Rb) and F atoms exhibit spherical charge contours along the (100) plane, manifesting the existence of ionic bonding between them (Figs. 6a, 7a). In addition, a covalent bonding nature of Ge–F is predicted, as the elliptical shape of charge distribution is observed around Ge and F atoms along the (200) plane (Figs. 6b, 7b). Charge density is also estimated at an applied pressure of 30 GPa to understand the effect of pressure on charge distribution. There is no noticeable difference in the spherical charge contours around K(Rb) and F atoms along the (100) plane (Figs. 6c, 7c). However, the contours around Ge and F atoms become more elliptical along the (200) plane, intensifying the covalent bonding of Ge–F (Figs. 6d, 7d). The bond length of Ge–F is longer than that of K(Rb)–F (Table 1), indicating strong bonding between K(Rb) and F atoms than that of bonding between Ge and F atoms. Therefore, the weaker covalent bond of Ge–F and stronger ionic bond of K(Rb)–F are exhibited in the crystal structure of $AGeF_3$ (A = K, Rb), which validates the estimated results predicted by charge density maps. The bond length decreases monotonically as pressure increases (Fig. S4a,b) and hence, the ionic/covalent bonds become stronger.

Optical properties. Metal halides without lead (non-toxic) have served as a source of interest due to their outstanding optical characteristics. They demonstrate much appreciated performance in optoelectronic devices

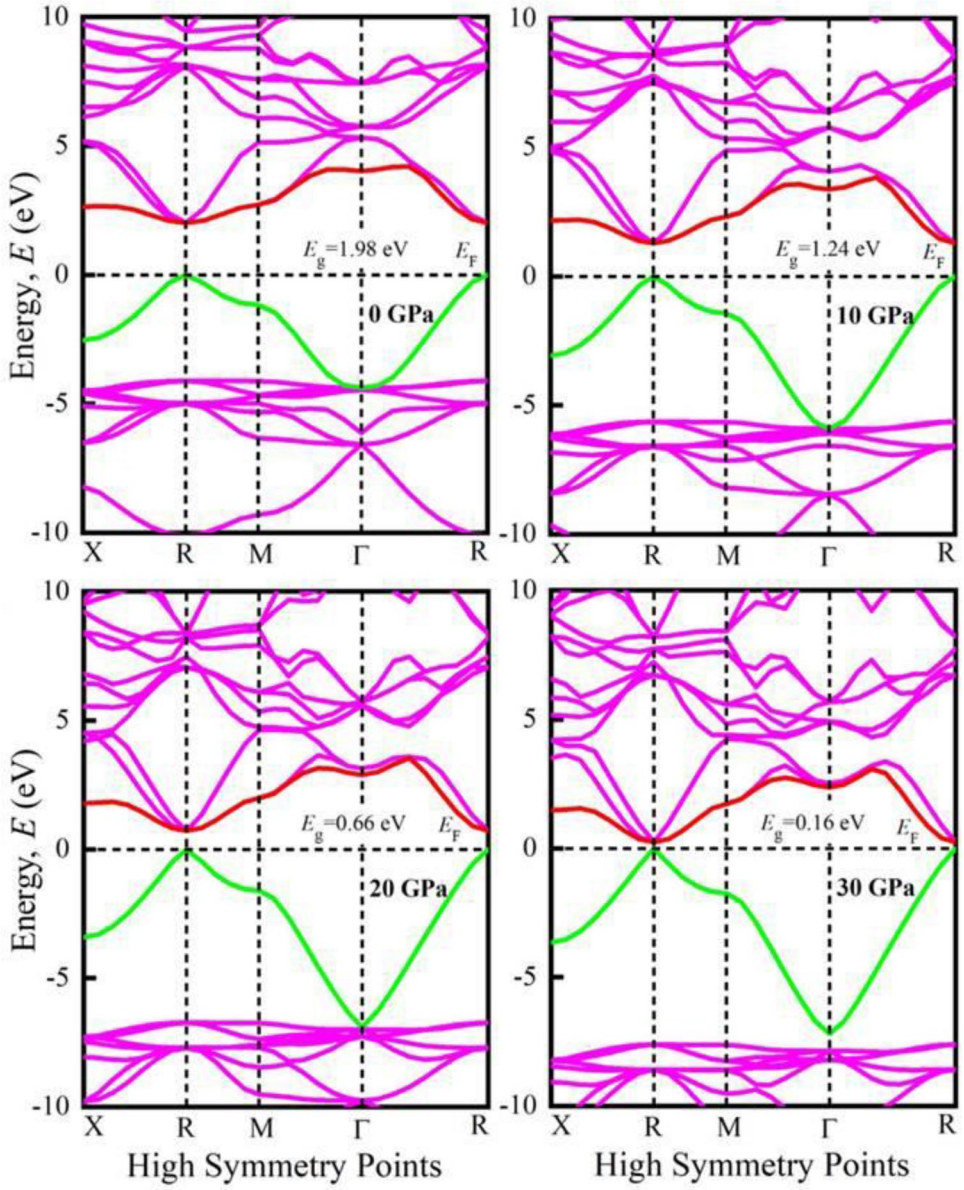

Figure 2. Band structures of $KGeF_3$ under applied pressure.

and photovoltaic cells. This section deeply analyzes and discusses a few optical characteristics, namely absorption, conductivity, reflectivity, reflective index, and dielectric function. The findings are presented using an electronic polarization vector of [100] at 0 GPa and 30 GPa pressures.

It is necessary to determine dielectric function to obtain rest of the optical functions[44]. It can be represented as $\varepsilon(\omega) = \varepsilon_1(\omega) + i\varepsilon_2(\omega)$; where $\varepsilon_1(\omega)$ and $\varepsilon_2(\omega)$ denote the real and imaginary parts of dielectric function, respectively[45]. According to Kramers–Kronig relation[46], $\varepsilon_1(\omega)$ is written as,

$$\varepsilon_1(\omega) = 1 + \frac{2}{\pi} P \int_0^\infty \frac{\omega' \varepsilon_2(\omega')}{\omega'^2 - \omega^2} d\omega'.$$

On the other hand, $\varepsilon_2(\omega)$ may also calculate using the momentum tensors between the occupied and unoccupied wave functions[47,48].

$$\varepsilon_2(\omega) = \frac{2e^2\pi}{\Omega\varepsilon_0} \sum_{K,V,C} \left| \langle \psi_k^c \left| \widehat{U} \cdot \vec{r} \right| \psi_k^V \rangle \right|^2 \delta(E_K^C - E_K^V - E).$$

Here, ω signifies the light frequency. ψ_k^c and ψ_k^V denote the conduction and valance band wave function at k, respectively, e is the electronic charge, Ω represents the unit cell volume, and U indicates the unit vector along the polarization of the incident electric field. The delta function ensures energy and momentum conservation

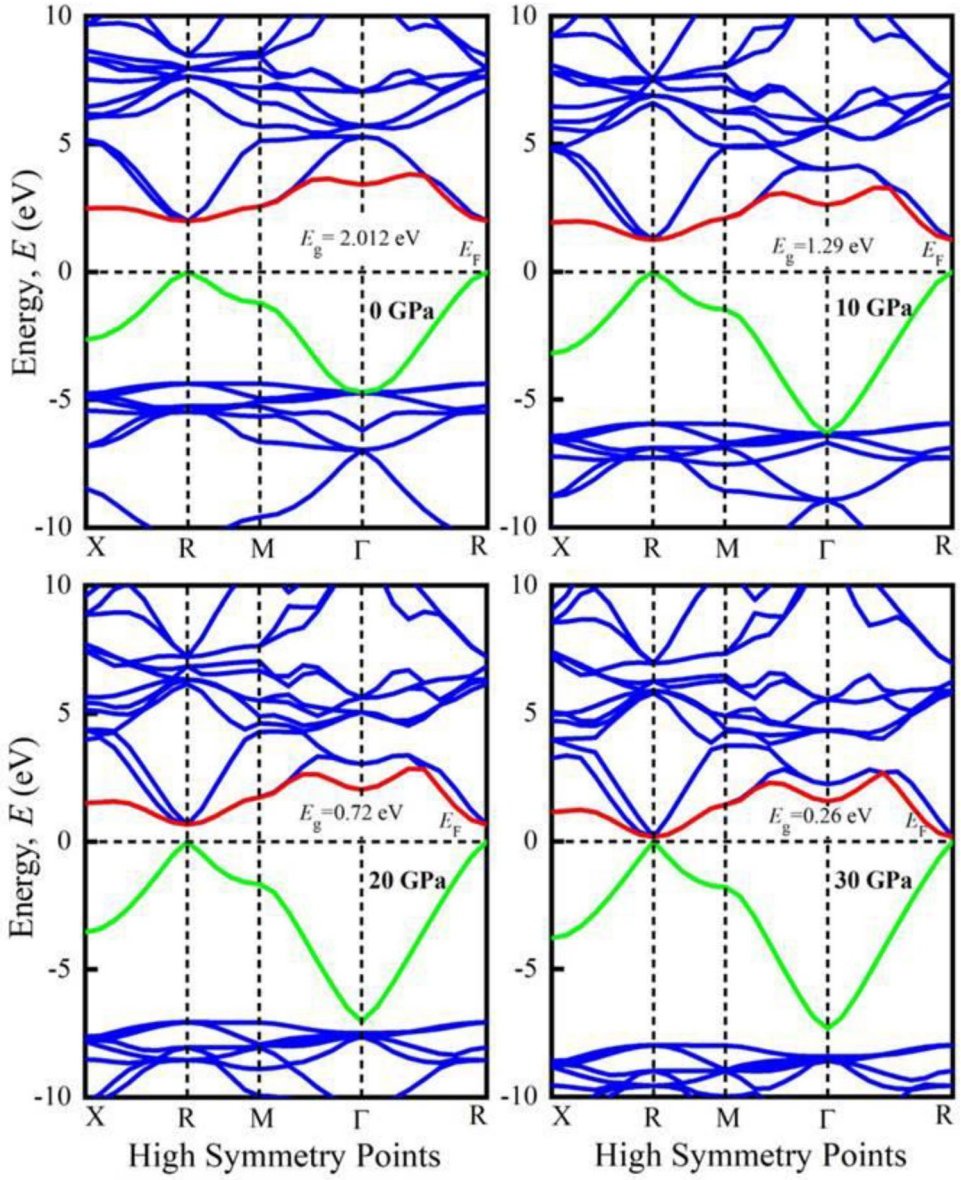

Figure 3. Band structures of $RbGeF_3$ under applied pressure.

during a transition between occupied and unoccupied electronic states through the emission or absorption of photon energy, *E*. E_K^C and E_K^V denote the energy of electrons at a certain *k*-vector in the conduction and valence bands, respectively. The rest of the optical parameters are calculated using the expressions given elsewhere[49].

The optical absorption coefficient (α) denotes the amount of energy absorbed by a substance per unit length. The efficiency of a material's optimal solar energy conversion can simply be described by it. From Fig. 8a, the absorption does not begin at 0 eV, since both $KGeF_3$ and $RbGeF_3$ contain a band gap at ambient pressure. In the ultraviolet region, $KGeF_3$ and $RbGeF_3$ show three sharp peaks in the range of ~ 8–22 eV and ~ 8–18 eV, respectively. So, both compounds work as good absorbers in the ultraviolet region at 0 GPa. When 30 GPa pressure is applied both compounds also show peaks within the ultraviolet region similar that exhibit at 0 GPa. In this case, both compounds show an additional peak at ~ 15 eV. Interestingly, the absorption spectra almost start from 0 eV (but not 0 eV due to having very small band gap) at 30 GPa (inset of Fig. 8a). The absorption in the visible light region is explicitly shown in Fig. 8b. The absorption of both compounds in the visible region is explicitly higher at 30 GPa than that observed at 0 GPa. As a result, the studied perovskites are expected to use visible light energy for photovoltaic conversion at a pressure of 30 GPa, potentially increasing the efficiency of solar cells.

Photoconductivity is another term of optical conductivity (σ). It refers to the conductivity of photons in a substance[50]. Figure 8c illustrates the σ of $AGeF_3$ (A = K, Rb) at 0 GPa and 30 GPa pressures. At 0 GPa, the perovskites exhibit σ in the visible area. The σ achieves its maximum value at negative $\varepsilon_1(\omega)$ (Fig. 9c). Therefore, $KGeF_3$ and $RbGeF_3$ show maximum σ in the energy region ~ 22–24 eV and ~ 18–22 eV, respectively. At 30 GPa, both compounds show increased σ in the visible region (Fig. 8d). Just like at 0 GPa, the highest σ peak of $KGeF_3$ is in

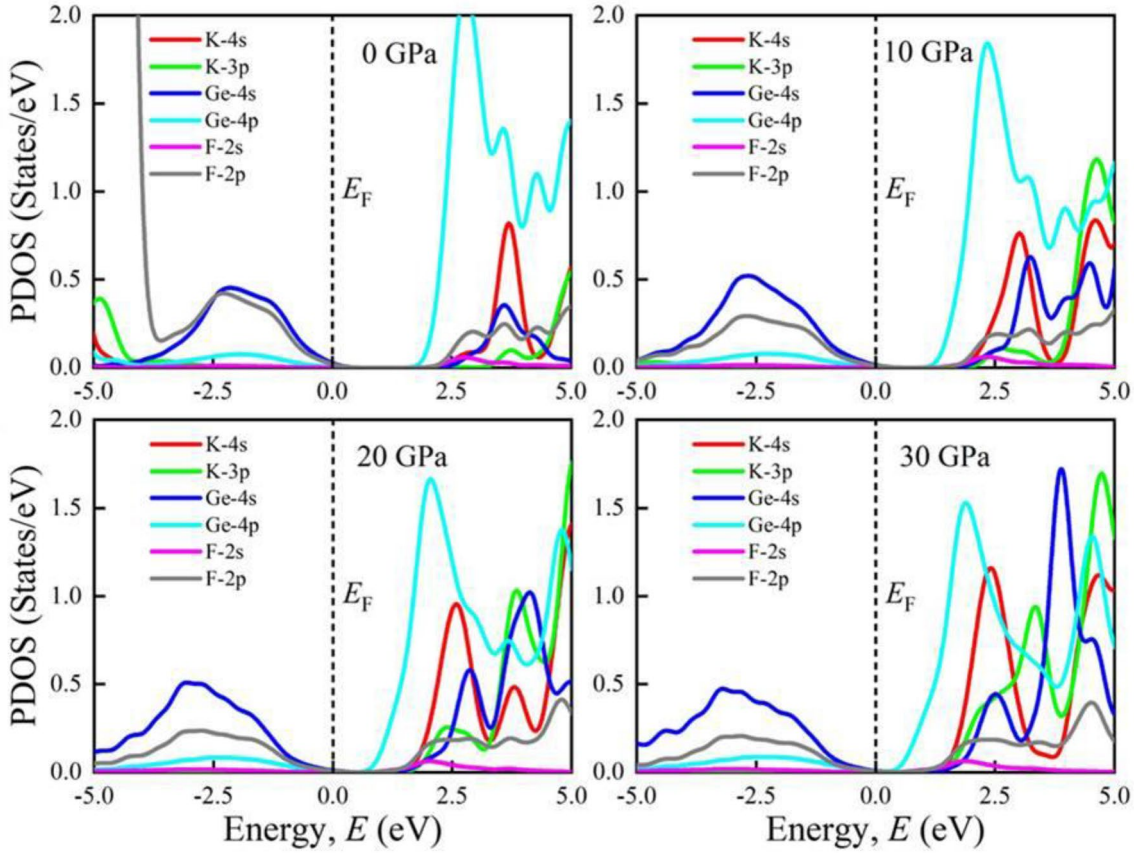

Figure 4. Partial density of states of $KGeF_3$ under applied pressure.

the energy region ~ 22–24 eV. But the highest σ peak slightly shifts to the energy range ~ 19–21 eV for $RbGeF_3$. However, the σ of both compounds significantly increases in the visible region under pressure as can be seen in Fig. 8d because of increased absorption.

The reflectivity (R) is a critical optical feature for material's photovoltaic applications. When exposed to photon with very low energy, $KGeF_3$ and $RbGeF_3$ reflect around 10% of the incident light (Fig. 9a). It rises for both substances when they transit from the infrared to the visible range. After transiting to the ultraviolet region, $KGeF_3$ and $RbGeF_3$ exhibit their highest R peak at ~ 23 eV and ~ 20 eV, where the dielectric function's real part is negative. Under 30 GPa pressure, the R of both compounds spikes to 20% at zero energy. The application of pressure increases the R of both materials throughout almost whole energy regions. However, the relatively lower R (with or without the application of pressure) at low energy region indicates the potentiality of both compounds in solar cell applications. Additionally, both compounds should be applied as coating material to minimize solar heating because of their higher R at high energy region[51].

The refractive index (n) is used to determine the amount of light bent or refracted as it enters into a substance. Furthermore, the phase velocity of an electromagnetic wave in a medium can also be calculated by n. According to Fig. 9b, both compound's n is prominent at low energy and showing a fluctuating nature in the high energy region. When 30 GPa pressure is applied, the n of both compounds significantly enhances at 0 eV. This implies that $AGeF_3$ (A = K, Rb) should be preferable for optical devices, like photonic crystals and waveguides[52].

The dielectric function characterizes the interaction of a material with incoming electromagnetic radiation. As a result, it is critical to have knowledge about dielectric function for optoelectronic device applications. The real (ε_1) and imaginary (ε_2) parts of dielectric function of $AGeF_3$ (A = K, Rb) are shown in Fig. 9c,d, respectively. The static dielectric function, ε_1 (0) is an important quantity, which measures the efficiency of an optoelectronic device[15]. A material with a greater ε_1 (0) has a lower rate of charge recombination, which results in improved performance of optoelectronic devices[52]. At ambient pressure, both compounds show identical ε_1 low energy, which enhances in the infrared–visible region and declines upon entering into the ultraviolet region. In addition, both $KGeF_3$ and $RbGeF_3$ show negative ε_1 at energy ranging from ~ 22 to 24 eV to ~ 18 to 22 eV, respectively. This implies that the compounds show high reflectivity at that energy region, which is evident in Fig. 9a. When 30 GPa pressure is applied, the ε_1 (0) is remarkably increased owing to the lower recombination of charges, which makes the compounds even more suitable for optoelectronic devices applications. At 0 GPa, the ε_2 is higher in the visible and early ultraviolet region, conveying high absorption at that regions[53]. But the spectrum of the ε_2 shifts to the low energy region at high pressure. Specifically, the larger ε_1 and ε_2 at low energy together with smaller ε_1 and ε_2 at high energy areas evident the feasibility of both compounds in microelectronics and integrated circuits[39], and the superiority is greatly enhanced under pressure.

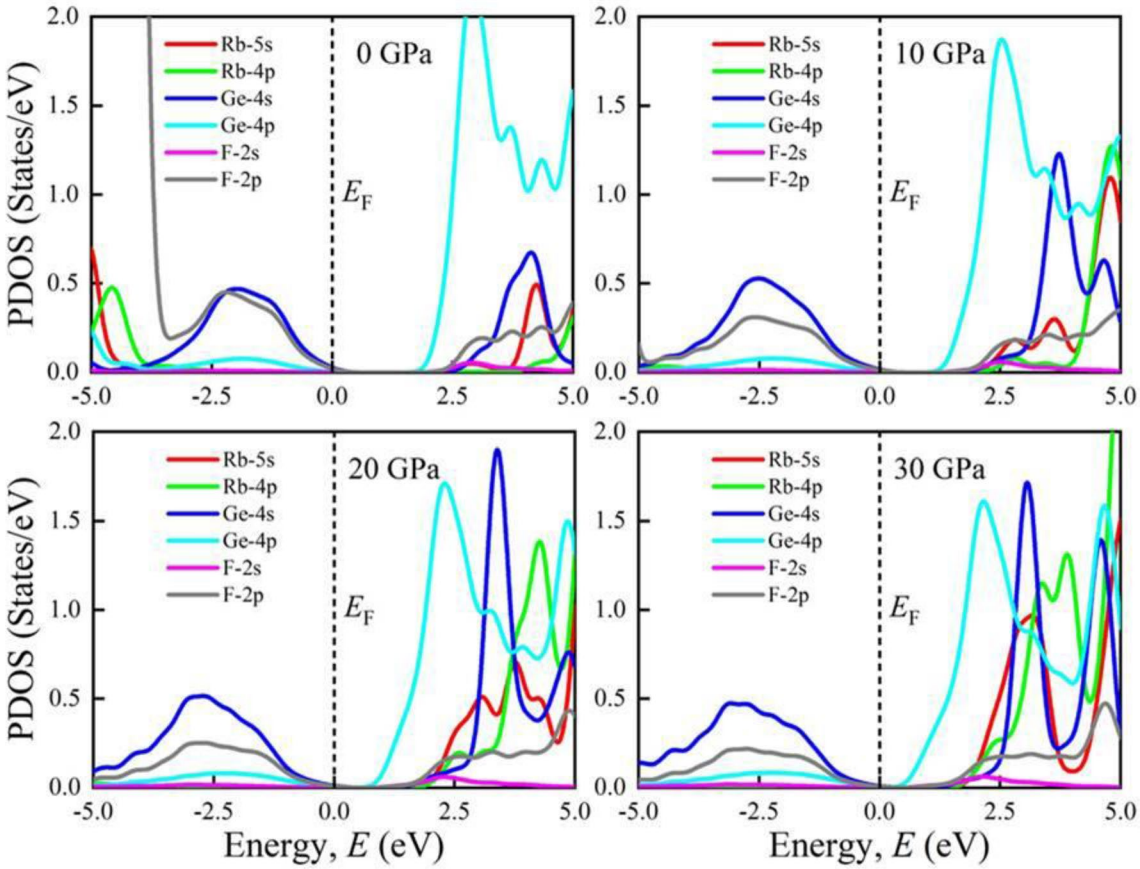

Figure 5. Partial density of states of $RbGeF_3$ under applied pressure.

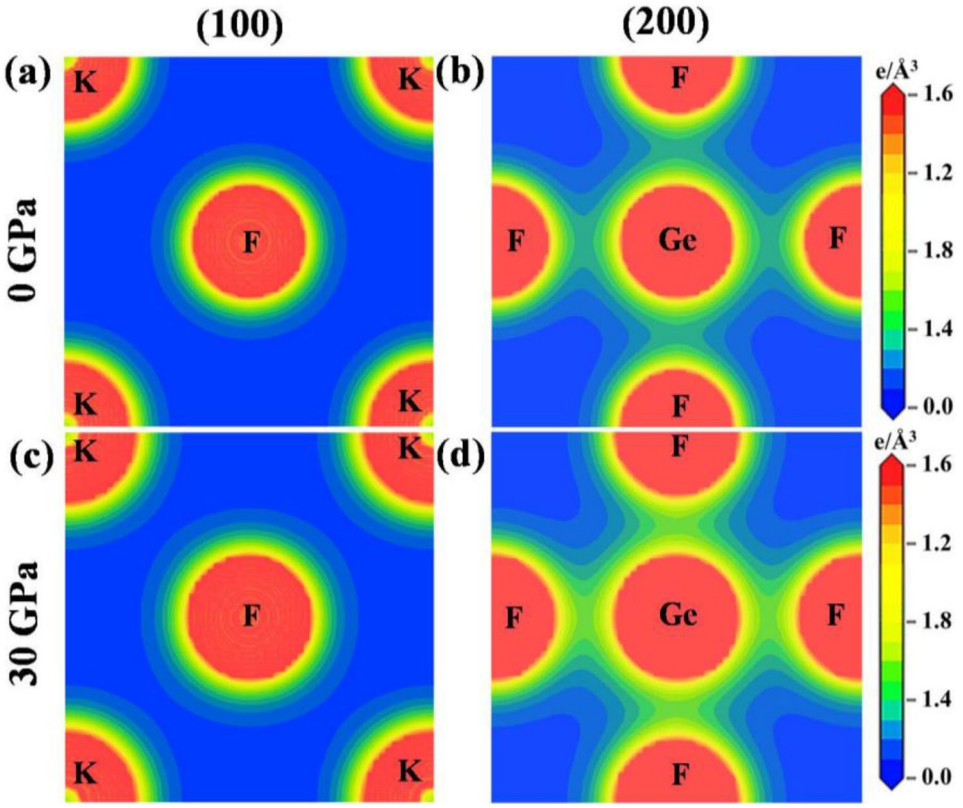

Figure 6. Charge density plots of $KGeF_3$ at 0 GPa and 30 GPa pressure.

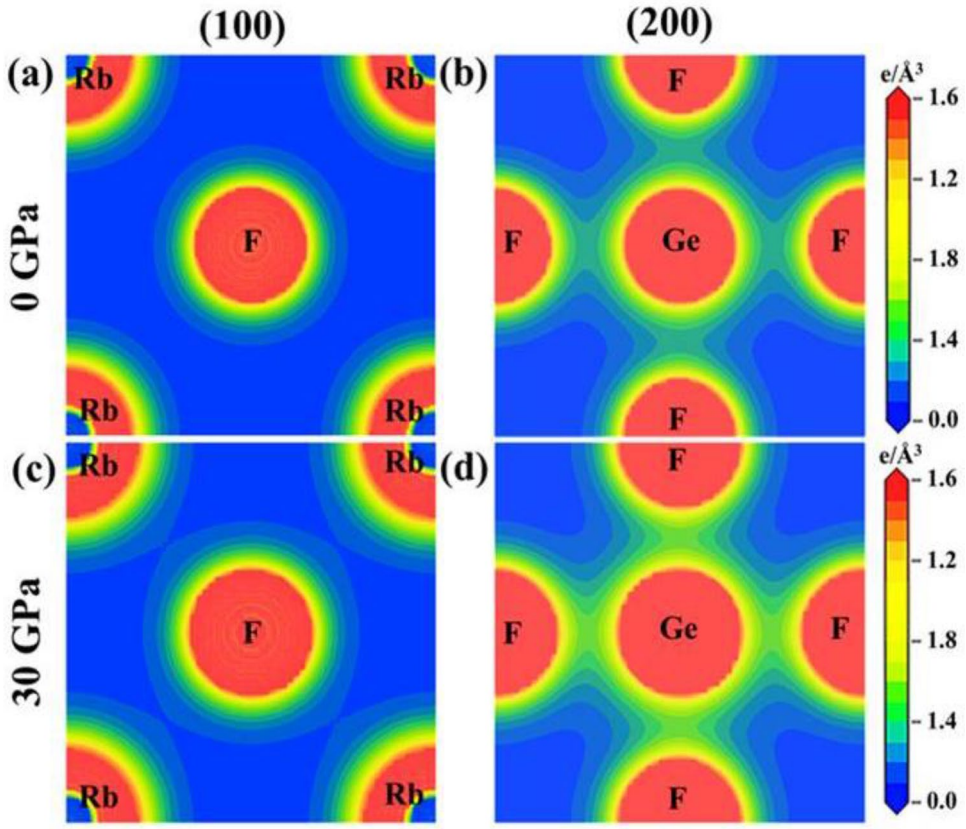

Figure 7. Charge density plots of $RbGeF_3$ at 0 GPa and 30 GPa pressure.

Mechanical properties. The elastic constants (C_{ij}) are usually used to determine the structural stability and mechanical characteristics of a material. The elastic nature describes how a material deforms under strain before recovering and returning to its original shape once the load is removed. It is important to reveal information about the binding properties between adjoining atomic planes, the anisotropic nature, and structural stability[54]. A cubic compound has three independent elastic constants: C_{11}, C_{12}, and C_{44}. Table 3 lists the computed C_{11}, C_{12}, C_{44}, and Cauchy pressure ($C_{12} - C_{44}$) for these two compounds under pressure. The elastic constants at ambient pressure are comparable with reported study[20] but rise linearly as pressure increases (Fig. S5a). Since the well-known Born stability requirements ($C_{44} > 0$, $C_{11} - C_{12} > 0$, and $C_{11} + 2C_{12} > 0$)[55] are nicely matched by all the calculated elastic constants, both the studied compounds are mechanically stable even under applied pressure. In addition, $C_{12} - C_{44}$ can identify the brittleness and ductility of materials. If $C_{12} - C_{44}$ possesses a positive (negative) value, the material should be ductile (brittle)[56]. Therefore, the titled compounds are expected to be ductile because of having positive values of $C_{12} - C_{44}$ (Table 3). However, $KGeF_3$ is slightly more ductility than that of $RbGeF_3$ (Table 3).

Various essential mechanical characteristics, such as bulk modulus (B), shear modulus (G), Young's modulus (E), Poisson's ratio (ν), Pugh's ratio (B/G), and Zener anisotropy index (A) of $AGeF_3$ (A = K, Rb) are determined using the estimated C_{ij} and presented in Table 4 with available reported data[20]. The B and G are determined using the Voigt–Reuss scheme. The Voigt and Reuss coefficients describe the upper and lower bounds of the effective modulus, respectively. For cubic lattices, the Voigt bulk modulus (B_V) and Voigt shear modulus (G_V) as well as the Reuss bulk modulus (B_R) and Reuss shear modulus (G_R) are described by the well-known expressions[57,58]. According to Hill's theory[59], the B and G are the arithmetic mean of Voigt and Reuss expressions. Furthermore, the E and ν are provided by the equations reported elsewhere[59]. The B and G stand for fracture resistant and plastic deformation, respectively. Because of having greater B and G, $RbGeF_3$ is more fracture and plastic deformation resistant than $KGeF_3$ (Fig. S5b). E is a measure of material's stiffness and has proportional relationship. As a result, $RbGeF_3$ will be stiffer than $KGeF_3$. However, the application of pressure induces more resistance to fracture and plastic deformation as well as makes them stiffer than that exhibited by the compounds without pressure. The variation of elastic moduli under applied pressure is graphically represented in Fig. S5b.

The critical value of ν to distinguish a materials' ductile or brittle nature is 0.26[60]. A material is said to be ductile if ν is larger than 0.26. Thus, both $KGeF_3$ and $RbGeF_3$ are concluded as ductile materials (Table 4). Another essential feature is B/G, which has a crucial value of 1.75 to divide solid materials into ductile or brittle[61]. The calculated values of B/G also reveal the ductile behavior of both compounds (Table 4). However, the ductility of $KGeF_3$ is slightly higher than that of $RbGeF_3$. The ductility of the studied compounds at 0 GPa has previously been predicted[20], which is consistent with this study. It seen from Figs. S6a,b that both ν and B/G, respectively, are

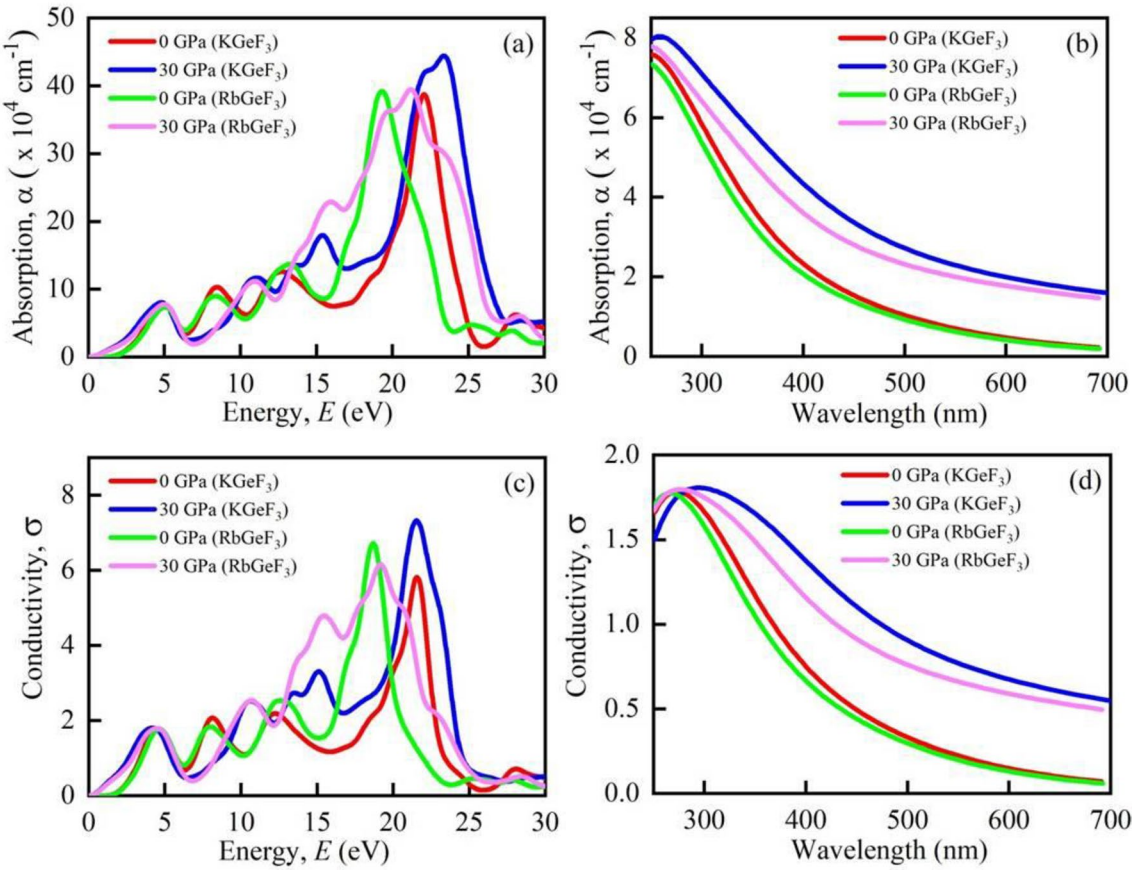

Figure 8. Calculated pressure induced optical **(a)** absorption vs. energy, **(b)** absorption vs. wavelength, **(c)** conductivity vs. energy, and **(d)** conductivity vs. wavelength of $AGeF_3$ (A = K, Rb).

increased with increasing pressure, which exhibit more ductile nature of the studied compounds under pressure. Interestingly, the outcome of v and B/G completely resemblances the data of $C_{12} - C_{44}$ (Tables 3, 4).

In applied engineering, the ability to observe the influence of elastic anisotropy on these features is critical[62]. The properties of a system may be directionally dependent and anisotropic index is used to calculate it. For example, the shear anisotropic factor is utilized to determine the degree of anisotropy in the bonding strength of atoms along different crystallographic planes. Three shear anisotropic factors A_1, A_2, and A_3 have been found along the (100), (010), and (001) planes, respectively[63]. For cubic systems, these are similar to the Zener anisotropy factor (A) and can be determined by the empirical formula[64]. An isotropic material must have the unit value of A and the departure of unity denotes anisotropy[65]. Both the compounds exhibit anisotropic nature, which are enhanced under pressure (Table 4). However, $KGeF_3$ show more anisotropy as compared to $KGeF_3$. Figure 10a–c show the direction dependence of E, G, and v, respectively, at 0 and 30 GPa pressure to highlight the anisotropic character of $KGeF_3$ and $RbGeF_3$. The isotropy of is represented by the spherical 3D plots, whereas anisotropy is revealed by non-spherical plots[7]. The elastic anisotropy of studied perovskites is appeared in all directions, as indicated by the non-spherical 3D contour plots. The deviation of spherical plots is more extreme at 30 GPa pressure than that exhibited at 0 GPa pressure, manifesting that the applied pressure may promote the anisotropy of $AGeF_3$ (A = K, Rb).

Conclusions

The physical characteristics of lead-free halide perovskites $AGeF_3$ (A = K, Rb) under hydrostatic pressure are investigated using DFT. The lattice constant and cell volume reveal similarities with available studies, but decrease with the application of pressure. With increased pressure, the band gap narrows considerably, resulting in improving optical functions and make the compounds suitable for solar cell applications. The ionic/covalent bonds in the compounds also become stronger under pressure. Both compounds exhibit ductile nature at ambient pressure, as determined by their Cauchy pressure, Poisson's ratio, and Pugh's ratio. The compounds become more ductile because of pressure effect. The anisotropic nature of both compounds demonstrates similar nature as ductility. At last, it can be expected that this literature will shed fresh light on the improvement of perovskite solar cells and their prospective applications.

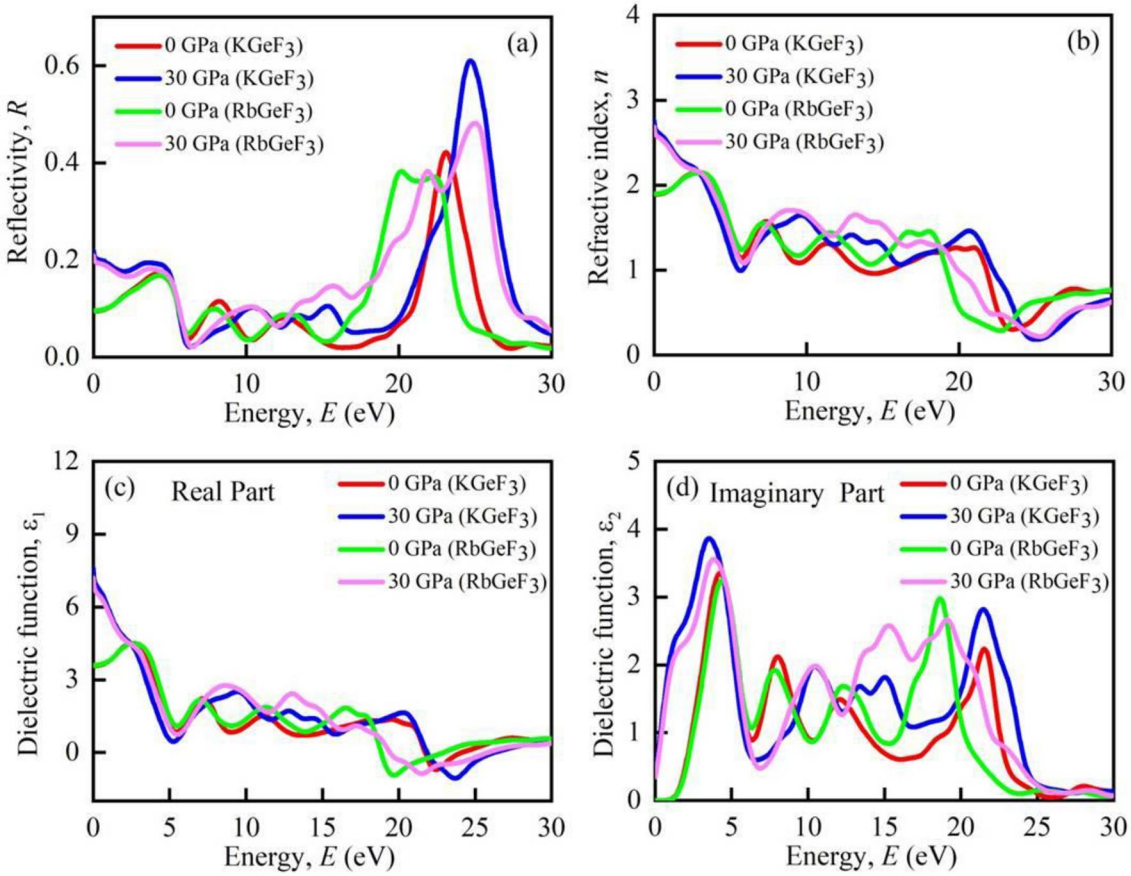

Figure 9. Calculated pressure induced spectra of optical **(a)** reflectivity, **(b)** refractive index, **(c)** real part of dielectric function, and **(d)** imaginary part of dielectric function of $AGeF_3$ (A = K, Rb).

Pressure (GPa)	Compound	C_{11}	C_{12}	C_{44}	$C_{12}-C_{44}$
0[31]	$KGeF_3$	80.67	35.57	5.96	29.61
	$RbGeF_3$	82.61	34.28	12.53	21.75
0	$KGeF_3$	93.66	30.17	13.07	17.10
	$RbGeF_3$	91.35	33.25	16.53	16.72
10	$KGeF_3$	165.95	52.47	10.22	42.25
	$RbGeF_3$	163.40	57.57	16.45	41.12
20	$KGeF_3$	233.93	77.25	6.66	70.59
	$RbGeF_3$	227.88	81.06	15.51	65.55
30	$KGeF_3$	293.88	98.42	2.51	95.91
	$RbGeF_3$	292.15	107.79	13.99	93.80

Table 3. Calculated elastic constants C_{ij} (GPa) and Cauchy pressure $C_{12}-C_{44}$ (GPa) of $AGeF_3$ (A = K, Rb) at various applied pressures.

Computational method

The present computations are done by Cambridge Serial Total Energy Package (CASTEP) grounded on density functional theory (DFT)[66]. The orbital shape approximations are not taken into account in the CASTEP code[67]. Though the compounds $KGeF_3$ and $RbGeF_3$ are yet to synthesize their crystal structure is constructed by taking the reported crystallographic data determined by the theoretical investigation[20]. Houari et al.[20] predicted that both compounds may have cubic perovskite-type structure with the space group *Pm*-3*m* (#221) as well as the lattice constant is 4.46 Å and 4.49 Å for $KGeF_3$ and $RbGeF_3$, respectively. The generalized gradient approximation (GGA) combined with Perdew–Berke–Emzerhof (PBE) functional is chosen to perform the exchange–correlation effect[68]. To evaluate the electron–ion interaction, the Vanderbilt-type ultrasoft pseudopotential is selected[69]. The cut off energy is 900 eV following a *k*-point grid of $12\times12\times12$. To sample the Brillouin zone, the Monkhorst–Pack scheme[70] is considered. The convergence tolerance factors are set as 5×10^{-6} eV/atom for total energy,

Pressure (GPa)	Compound	*B*	*G*	*E*	*B*/*G*	*v*	*A*
0[31]	$KGeF_3$	50.61	10.52	29.53	4.81	0.40	0.26
	$RbGeF_3$	50.39	16.35	44.27	3.08	0.35	0.52
0	$KGeF_3$	51.34	18.81	50.30	2.73	0.366	0.412
	$RbGeF_3$	52.62	20.76	55.03	2.49	0.326	0.569
10	$KGeF_3$	90.30	22.01	61.08	4.10	0.387	0.180
	$RbGeF_3$	92.97	26.85	73.47	3.46	0.368	0.311
20	$KGeF_3$	129.4	22.92	64.93	5.65	0.416	0.085
	$RbGeF_3$	130.00	30.67	85.29	4.24	0.391	0.211
30	$KGeF_3$	163.57	22.35	64.14	7.32	0.434	0.026
	$RbGeF_3$	169.24	33.22	93.55	5.09	0.407	0.152

Table 4. The calculated bulk modulus *B* (GPa), shear modulus *G* (GPa), Young's modulus *E* (GPa), Poisson's ratio *v*, Pugh's ratio *B*/*G*, and Zener anisotropy index *A* of $AGeF_3$ (A = K, Rb) at various applied pressures.

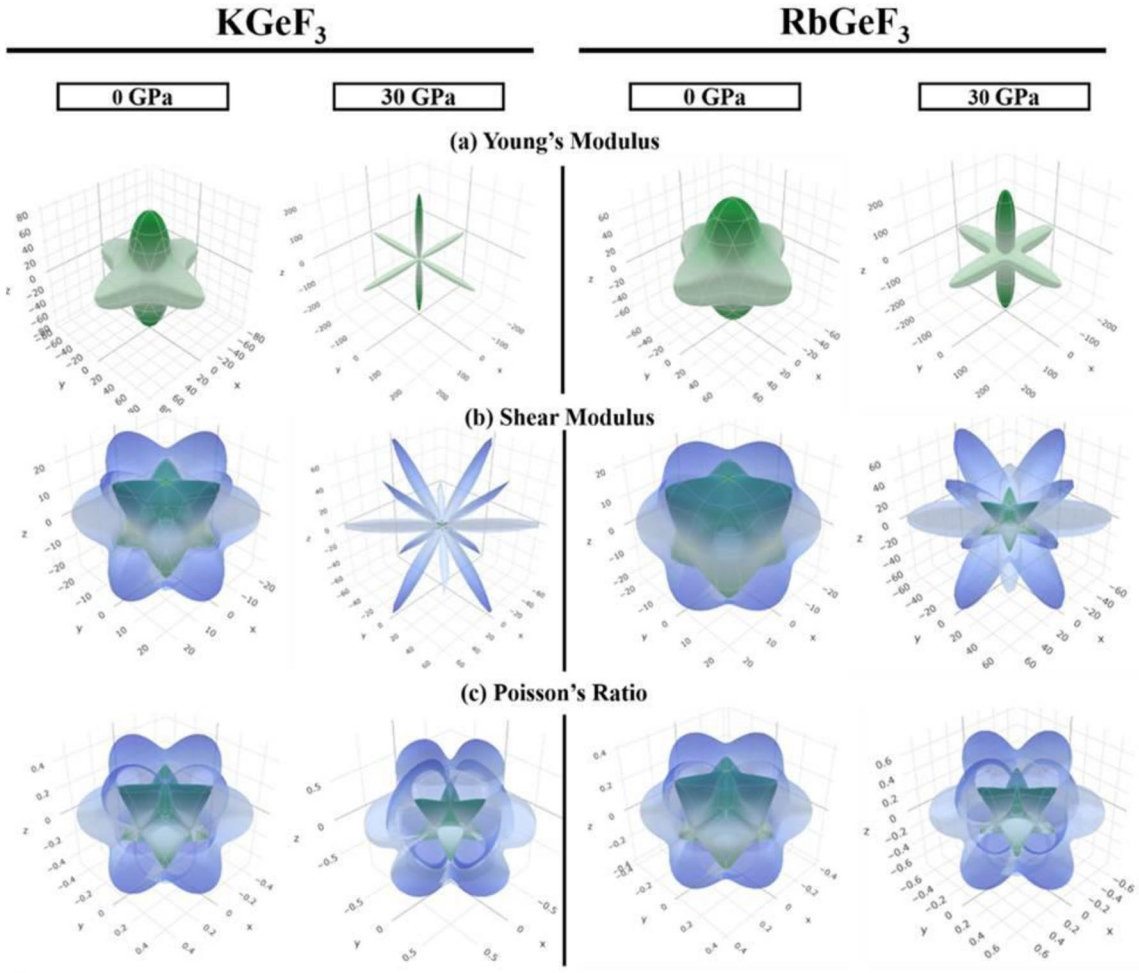

Figure 10. Anisotropic 3D representation of **(a)** Young's modulus, **(b)** shear modulus, and **(c)** Poisson's ratio of $AGeF_3$ (A = K, Rb) at 0 and 30 GPa pressure.

5×10^{-4} Å for maximum displacement, 0.01 eV/Å for maximum force, and 0.02 GPa for maximum stress. The Broyden–Fletcher–Goldferb–Shanno (BFGS) algorithm[71] is employed to optimize the crystal structure. The relatively similar approximations were also employed to optimize the crystal structure of experimentally synthesized Pb-based and Pb-free cubic halide perovskites[39,72–74]. In this study, the hydrostatic pressure up to 30 GPa with an interval of 10 GPa is applied during structural optimization. The optimized crystal structure is constructed by VESTA software[75]. The electronic and optical properties are calculated by using the same parameters that are utilized in structural optimization. The elastic constants and elastic moduli are determined by "stress–strain" method[76] embodied in the CASTEP code. The ELATE program[77] is used to create the three-dimensional (3D) anisotropic contour plots of Young's modulus, shear modulus, and Poisson's ratio.

Data availability

The datasets generated and/or analyzed in this study are available from the corresponding author upon reasonable request.

Received: 18 February 2022; Accepted: 9 May 2022
Published online: 23 May 2022

References

1. Bisquert, J. *The Physics of Solar Cells: Perovskites, Organics, and Photovoltaic Fundamentals* (CRC Press, 2017).
2. He, T. *et al.* Superconductivity in the non-oxide perovskite $MgCNi_3$. *Nature* **411**, 54–56 (2001).
3. Eperon, G. E. *et al.* Inorganic caesium lead iodide perovskite solar cells. *J. Mater. Chem. A* **3**, 19688–19695 (2015).
4. Saiduzzaman, M. *et al.* Hydrothermal synthesis and crystal structure of a $(Ba_{0.54}K_{0.46})_4Bi_4O_{12}$ double-perovskite superconductor with onset of the transition $T_c \sim 30$ K. *Inorg. Chem.* **58**, 11997–12001 (2019).
5. Hossain, K. M., Saiduzzaman, M., Kumada, N., Takei, T. & Yamane, H. Hydrothermal synthesis and crystal structure of a novel double-perovskite-type bismuth oxide with 3:1 ordering at the B-site. *New J. Chem.* **46**, 3595–3601 (2022).
6. Hossain, K. M., Hasan, M. Z. & Ali, M. L. Narrowing bandgap and enhanced mechanical and optoelectronic properties of perovskite halides: Effects of metal doping. *AIP Adv.* **11**, 015052 (2021).
7. Biswas, A. *et al.* Effects of Bi and Mn codoping on the physical properties of barium titanate: Investigation via DFT method. *Appl. Phys. A* **127**, 939 (2021).
8. Yangb, W. S. *et al.* Iodide management in formamidinium-lead-halide-based perovskite layers for efficient solar cells. *Science* **356**, 1376–1379 (2017).
9. NREL. *Pv Research Cell Record Efficiency. Chart* (2019).
10. Ava, T. T., Mamun, A. A., Marsillac, S. & Namkoong, G. A review: Thermal stability of methylammonium lead halide based perovskite solar cells. *Appl. Sci.* **1**, 188 (2019).
11. Nishimura, K. *et al.* Lead-free tin-halide perovskite solar cells with 13% efficiency. *Nano Energy* **74**, 104858 (2020).
12. Yuan, Y. *et al.* Nature of the band gap of halide perovskites ABX_3 (A = CH_3NH_3, Cs; B = Sn, Pb; X = Cl, Br, I): First-principles calculations. *Chin. Phys. B* **24**, 116302 (2015).
13. Zhao, T., Zhang, S., Guo, Y. & Wang, Q. TiC_2: A new two-dimensional sheet beyond MXenes. *Nanoscale* **8**, 233–242 (2016).
14. Roknuzzaman, M. *et al.* Insight into lead-free organic-inorganic hybrid perovskites for photovoltaics optoelectronics: A first-principles study. *Org. Electron.* **59**, 99–106 (2018).
15. Zuo, X. *et al.* Bubble-template-assisted synthesis of hollow fullerene-like MoS_2 nanocages as a lithium ion battery anode material. *J. Mater. Chem. A* **4**, 51–58 (2016).
16. Berhe, T. A. *et al.* Organometal halide perovskite solar cells: Degradation and stability. *Energy Environ. Sci.* **9**, 323–356 (2016).
17. Protesescu, L. *et al.* Nanocrystals of cesium lead halide perovskites ($CsPbX_3$, X = Cl, Br, I): Novel optoelectronic materials showing bright emission with wide color gamut. *Nano Lett.* **15**, 3692–3696 (2015).
18. Swarnkar, A. *et al.* Quantum dot-induced phase stabilization of α-$CsPbI_3$ perovskite for high-efficiency photovoltaics. *Science* **354**, 92–95 (2016).
19. Kovalsky, A., Wang, L., Marek, G. T., Burda, C. & Dyck, J. S. Thermal conductivity of $CH_3NH_3PbI_3$ and $CsPbI_3$: Measuring the effect of the methylammonium ion on phonon scattering. *J. Phys. Chem. C* **121**, 3228–3233 (2017).
20. Houari, M. *et al.* Semiconductor behavior of halide perovskites $AGeX_3$ (A = K, Rb, Cs; X = F, Cl, Br): First principles calculations. *Indian J. Phys.* **94**, 455–467 (2020).
21. Stoumpos, C. C. *et al.* Hybrid germanium iodide perovskite semiconductors: Active lone pairs, structural distortions, direct indirect energy gaps, and strong nonlinear optical properties. *J. Am. Chem. Soc.* **137**, 6804–6819 (2015).
22. Hamideddine, I., Zitouni, H., Tahiri, N., El Bounagui, O. & Ez-Zahraouy, H. A DFT study of the electronic structure, optical, thermoelectric properties of halide perovskite $KGeI_{3-x}Br_x$ materials: Photovoltaic applications. *Appl. Phys. A* **127**, 443 (2021).
23. Mao, X. *et al.* First-principles screening of all-inorganic lead-free ABX_3 perovskites. *J. Phys. Chem. C* **14**, 7670–7675 (2018).
24. Jiang, J., Onwudinanti, C. K., Hatton, R. A., Bobbert, P. A. & Tao, S. Stabilizing lead-free all-inorganic tin halide perovskites by ion exchange. *J. Phys. Chem. C* **122**, 17660–17667 (2018).
25. Khan, K., Sahariya, J. & Soni, A. Structural, electronic optical modeling of perovskite solar materials $ASnX_3$ (A = Rb, K; X = Cl, Br): First principle investigations. *Mater. Chem. Phys.* **262**, 124284 (2021).
26. Mahmood, Q. *et al.* The first-principle study of mechanical, optoelectronic and thermoelectric properties of $CsGeBr_3$ and $CsSnBr_3$ perovskites. *Mater. Res. Express* **6**, 045901 (2019).
27. Wang, Y. *et al.* Pressure induced phase transformation, reversible amorphization, and anomalous visible light response in organolead bromide perovskite. *J. Am. Chem. Soc.* **137**, 11144–11149 (2015).
28. Wang, L., Wang, K. & Zou, B. Pressure-induced structural and optical properties of organometal halide perovskite-based formamidinium lead bromide. *J. Phys. Chem. Lett.* **7**, 2556–2562 (2016).
29. Yuan, G., Qin, S., Wu, X., Ding, H. & Lu, A. Pressure-induced phase transformation of $CsPbI_3$ by X-ray diffraction and Raman spectroscopy. *Phase Transit.* **91**, 38–47 (2018).
30. Liu, D., Li, Q., Jing, H. & Wu, K. Pressure-induced effects in the inorganic halide perovskite $CsGeI_3$. *RSC Adv.* **9**, 3279–3284 (2019).
31. Huang, Y., Wang, L., Ma, Z. & Wang, F. Pressure-induced band structure evolution of halide perovskites: A first-principles atomic and electronic structure study. *J. Phys. Chem. C* **123**, 739–745 (2019).
32. Swainson, I. P., Tucker, M. G., Wilson, D. J., Winkler, B. & Milman, V. Pressure response of an organic-inorganic perovskite: Methylammonium lead bromide. *Chem. Mater.* **19**, 2401–2405 (2007).
33. Zhao, Q. *et al.* Size-dependent lattice structure and confinement properties in $CsPbI_3$ perovskite nanocrystals: Negative surface energy for stabilization. *ACS Energy Lett.* **5**, 238–247 (2020).
34. Talanov, M. V., Shirokov, V. B. & Talanov, V. M. Anion order in perovskites: A grouptheoretical analysis. *Acta. Crystallogr. A Found. Adv.* **72**, 222–235 (2016).
35. King, G. & Woodward, P. M. Cation ordering in perovskites. *J. Mater. Chem.* **20**, 5785 (2010).
36. Wang, F., Tan, M., Li, C., Niu, C. & Zhao, X. Unusual pressure-induced electronic structure evolution in organometal halide perovskite predicted from first-principles. *Org. Electron.* **67**, 89–94 (2019).
37. Ter-Oganessian, N. V. & Sakhnenko, V. P. Effect of pressure on the order-disorder phase transitions of B cations in $AB'_{1/2}B''_{1/2}O_3$ perovskites. *Acta Crystallogr. B Struct. Sci. Cryst. Eng. Mater.* **75**, 1034–1041 (2019).
38. Lin, J. *et al.* Pressure-induced semiconductor-to-metal phase transition of a charge-ordered indium halide perovskite. *PNAS* **116**, 23404–23409 (2019).
39. Haq, M. A., Saiduzzaman, M., Asif, T. I., Shuvo, I. K. & Hossain, K. M. Ultra-violet to visible band gap engineering of cubic halide $KCaCl_3$ perovskite under pressure for optoelectronic applications: Insights from DFT. *RSC Adv.* **11**, 36367–36378 (2021).
40. Ullah, R. *et al.* Structural, electronic and optical properties of cubic perovskite $RbYbF_3$ under pressure: A first principles study. *Mater. Res. Express* **6**, 125901 (2019).

41. Islam, M. A., Islam, J., Islam, M. N., Sen, S. K. & Hossain, A. K. M. K. Enhanced ductility and optoelectronic properties of environment-friendly $CsGeCl_3$ under pressure. *AIP Adv.* **11**, 045014 (2021).
42. Pan, Y. & Chen, S. Influence of alloying elements on the mechanical and thermodynamic properties of ZrB_2 boride. *Vacuum* **198**, 110898 (2022).
43. Gillani, S. S. A. *et al.* Effect of external pressure on the structural stability, electronic structure, band gap engineering and optical properties of $LiNbO_3$: An ab-initio calculations. *Mater. Today Commun.* **23**, 100919 (2020).
44. Mubarak, A. A. The first-principle study of the electronic, optical thermoelectric properties of $XTiO_3$ (X = Ca, Sr, Ba) compounds. *Int. J. Mod. Phys. B* **30**, 1650141 (2016).
45. Babu, K. E., Veeraiah, A., Swamy, D. T. & Veeraiah, V. First-principles study of electronic structure optical properties of cubic perovskite $CsCaF_3$. *Chin. Phys. Lett.* **29**, 117102 (2012).
46. Green, M. A., Jiang, Y., Soufiani, A. M. & Ho-Baillie, A. Optical properties of photovoltaic organic–inorganic lead halide perovskites. *J. Phys. Chem. Lett.* **6**, 4774–4785 (2015).
47. Draxl, C. A. & Sofo, J. O. Linear optical properties of solids within the full-potential linearized augmented plane wave method. *Comput. Phys. Commun.* **175**, 1–14 (2006).
48. Smith, N. V. Photoelectron energy spectra the band structures of the noble metals. *Phys. Rev. B* **3**, 1862–1878 (1971).
49. Hadi, M. A., Vovk, R. V. & Chroneos, A. Physical properties of the recently discovered $Zr_2(Al_{1-x}Bi_x)C$ MAX phases. *J. Mater. Sci. Mater. Electron.* **27**, 11925–11933 (2016).
50. Yu, G., Lee, C. H., Heeger, A. J. & Cheong, S. W. Photoconductivity optical conductivity in lightly doped $Nd_2CuO_{4-\delta}$. *Phys. C Supercond.* **203**, 419–425 (1992).
51. Li, S., Ahuja, R., Barsoum, M. W., Jena, P. & Johansson, B. Optical properties of Ti_3SiC_2 and Ti_4AlN_3. *Appl. Phys. Lett.* **92**, 221907 (2008).
52. Rahaman, M. Z. & Hossain, A. K. M. A. Effect of metal doping on the visible light absorption, electronic structure mechanical properties of non-toxic metal halide $CsGeCl_3$. *RSC Adv.* **8**, 33010–33018 (2018).
53. Rahaman, M. Z. & Rahman, M. A. Investigation of the physical properties of two laves phase compounds HRh_2 (H = Ca, La): A DFT study. *Int. J. Mod. Phys. B* **32**, 1850149 (2018).
54. Litimein, F., Khenata, R., Bouhemadou, A., Al-Douri, Y. & Omran, S. B. First-principle calculations to investigate the elastic thermodynamic properties of $RBRh_3$ (R = Sc, Y, La) perovskite compounds. *Mol. Phys.* **110**, 121–128 (2012).
55. Mouhat, F. & Coudert, F. X. Necessary sufficient elastic stability conditions in various crystal systems. *Phys. Rev. B* **90**, 224104 (2014).
56. Pettifor, D. G. Theoretical predictions of structure related properties of intermetallics. *Mater. Sci. Technol.* **8**, 345–349 (1992).
57. Naher, M. I. & Naqib, S. H. Structural, elastic, electronic, bonding, optical properties of topological $CaSn_3$ semimetal. *J. Alloys Compd.* **829**, 154509 (2020).
58. Al-Fahdi, M., Rodriguez, A., Ouyang, T. & Hu, M. High-throughput computation of new carbon allotropes with diverse hybridization ultrahigh hardness. *Curr. Comput.-Aided Drug Des.* **11**, 783 (2021).
59. Hill, R. The elastic behaviour of a crystalline aggregate. *Proc. Phys. Soc. A* **65**, 349–354 (1952).
60. Frantsevich, I. N., Voronov, F. F. & Bakuta, S. A. *Handbook on Elastic Constants and Moduli of Elasticity for Metals and Nonmetals* (Naukova Dumka, 1982).
61. Pugh, S. F. Relations between the elastic moduli and the plastic properties of polycrystalline pure metals. *Lond. Edinb. Dublin Philos. Mag. J. Sci.* **45**, 823–843 (1954).
62. Kube, C. M. Elastic anisotropy of crystals. *AIP Adv.* **6**, 095209 (2016).
63. Gao, X., Jiang, Y., Zhou, R. & Feng, J. Stability elastic properties of Y-C binary compounds investigated by first principles calculations. *J. Alloys Compd.* **587**, 819–826 (2014).
64. Zener, C. M. & Siegel, S. Elasticity and anelasticity of metals. *J. Phys. Colloid Chem.* **53**, 1468 (1949).
65. Mitro, S. K., Saiduzzaman, M., Biswas, A., Sultana, A. & Hossain, K. M. Electronic phase transition and enhanced optoelectronic performance of lead-free halide perovskites $AGeI_3$ (A = Rb, K) under pressure. *Mater. Today Commun.* **31**, 103532 (2022).
66. Payne, M. C., Teter, M. P., Allan, D. C., Arias, T. A. & Joannopoulos, J. D. Iterative minimization techniques for ab initio total-energy calculations: Molecular dynamics and conjugate gradients. *Rev. Mod. Phys.* **64**, 1045 (1992).
67. Segall, M. D. *et al.* First-principles simulation: Ideas, illustrations and the CASTEP code. *J. Phys. Condens. Matter* **14**, 2717–2744 (2002).
68. Perdew, J. P., Burke, K. & Ernzerhof, M. Generalized gradient approximation made simple. *Phys. Rev. Lett.* **77**, 3865–3868 (1996).
69. Vanderbilt, D. Soft self-consistent pseudopotentials in a generalized eigenvalue formalism. *Phys. Rev. B* **41**, 7892–7895 (1990).
70. Monkhorst, J. & Pack, J. D. Special points for Brillouin-zone integrations. *Phys. Rev. B* **13**, 5188–5192 (1976).
71. Fischer, T. H. & Almlof, J. General methods for geometry wave function optimization. *J. Phys. Chem.* **96**, 9768–9774 (1992).
72. Roknuzzaman, M., Ostrikov, K., Wang, H., Du, A. & Tesfamichael, T. Towards lead-free perovskite photovoltaics and optoelectronics by ab-initio simulations. *Sci. Rep.* **7**, 14024 (2017).
73. Shuvo, I. K., Saiduzzaman, M., Asif, T. I., Haq, M. A. & Hossain, K. M. Band gap shifting of halide perovskite $CsCaBr_3$ from ultraviolet to visible region under pressure for photovoltaic applications. *Mater. Sci. Eng. B* **278**, 115645 (2022).
74. Molla, M. R., Saiduzzaman, M., Asif, T. I., Dujana, W. A. & Hossain, K. M. Electronic phase transition from semiconducting to metallic in cubic halide $CsYbCl_3$ perovskite under hydrostatic pressure. *Physica B* **630**, 413650 (2022).
75. Momma, K. & Izumi, F. VESTA 3 for three-dimensional visualization of crystal, volumetric and morphology data. *J. Appl. Crystallogr.* **44**, 1272–1276 (2011).
76. Boekelheide, Z. *et al.* Antiferromagnetism in Cr_3Al relation to semiconducting behavior. *Phys. Rev. B* **85**, 094413 (2012).
77. Gaillac, R., Pullumbi, P. & Coudert, F. X. ELATE: An open-source online application for analysis and visualization of elastic tensors. *J. Phys. Condens. Matter* **28**, 275201 (2016).

Author contributions

M.S.A.: Investigation, methodology, data curation, writing the original draft. M.S.: Formal analysis, conceptualization, writing the original draft, supervision, reviewing, and editing. A.B., T.A., A.S.: Formal analysis, data curation. K.M.H.: Formal analysis, validation, writing the original draft, supervision, reviewing, and editing.

Competing interests

The authors declare no competing interests.

Additional information

Supplementary Information The online version contains supplementary material available at https://doi.org/10.1038/s41598-022-12713-4.

Correspondence and requests for materials should be addressed to M.S. or K.M.H.